PHYSICS

Three-dimensional femtosecond snapshots of isolated faceted nanostructures

Alessandro Colombo[1]*, Simon Dold[2], Patrice Kolb[1], Nils Bernhardt[3], Patrick Behrens[3], Jonathan Correa[4], Stefan Düsterer[4], Benjamin Erk[4], Linos Hecht[1], Andrea Heilrath[3], Robert Irsig[5], Norman Iwe[5], Jakob Jordan[3], Björn Kruse[5], Bruno Langbehn[3], Bastian Manschwetus[4], Franklin Martinez[5], Karl-Heinz Meiwes-Broer[5,6], Kevin Oldenburg[5], Christopher Passow[4], Christian Peltz[5], Mario Sauppe[1,3], Fabian Seel[3], Rico Mayro P. Tanyag[3], Rolf Treusch[4], Anatoli Ulmer[3], Saida Walz[3], Thomas Fennel[5], Ingo Barke[5,6], Thomas Möller[3], Bernd von Issendorff[7,8], Daniela Rupp[1,9]

The structure and dynamics of isolated nanosamples in free flight can be directly visualized via single-shot coherent diffractive imaging using the intense and short pulses of x-ray free-electron lasers. Wide-angle scattering images encode three-dimensional (3D) morphological information of the samples, but its retrieval remains a challenge. Up to now, effective 3D morphology reconstructions from single shots were only achieved via fitting with highly constrained models, requiring a priori knowledge about possible geometries. Here, we present a much more generic imaging approach. Relying on a model that allows for any sample morphology described by a convex polyhedron, we reconstruct wide-angle diffraction patterns from individual silver nanoparticles. In addition to known structural motives with high symmetries, we retrieve imperfect shapes and agglomerates that were not previously accessible. Our results open unexplored routes toward true 3D structure determination of single nanoparticles and, ultimately, 3D movies of ultrafast nanoscale dynamics.

INTRODUCTION

Coherent diffractive imaging (CDI) is a lensless technique that exploits the interference effects of coherent radiation scattered by an isolated sample to retrieve its spatial properties (1–5). A highly intense light beam intercepts the specimen of interest, and the intensity of the diffracted light is collected by a two-dimensional (2D) detector in far-field condition. CDI does not make use of optical devices, and its achievable spatial resolution is, in principle, only limited by the radiation wavelength. Thus, it is capable of fully exploiting the high-intensity ultrashort light pulses provided by the recently available free-electron lasers (FELs) to image isolated nanosamples. Examples range from biologically relevant specimen such as single viruses (4, 6) or macromolecules (7) to atomic clusters (8–10), nanocrystals (11), and even such fragile and short-lived structures as aerosols (12) or superfluid helium nanodroplets (13, 14). The extremely short pulses further allow time-resolved imaging of ultrafast dynamics in isolated nanoscale structures, which has opened up unprecedented possibilities for light-matter interaction studies (15–24).

CDI experiments can be roughly divided into two regimes defined by the angle upon which diffraction signal can be acquired. In the small-angle regime, the maximum scattering angle reaches up to only a few degrees, and correspondingly, the maximum transferred momentum is much smaller than the wave vector of the incident radiation (11). In this case, the diffraction pattern is proportional to the square amplitude of the Fourier transform of the 2D sample density, projected onto the plane orthogonal to the beam (25). The field phase, lost in the acquisition process, can be effectively recovered by so-called phase-retrieval algorithms (4, 26–30), which then allow the reconstruction of the sample's projected density. 3D reconstruction of samples can also be achieved in the small-angle range by tomographic approaches, i.e., by combining 2D projections of the same object or identical replicas in different orientations (31–35). However, for the investigation of isolated systems with intense FEL pulses, this approach is practicable only in special cases (6, 36–38) and unsuitable for dynamic investigations.

3D features of the sample are, on the other hand, naturally encoded in a single diffraction image acquired in the wide-angle regime. In this case, the maximum acquired transferred momentum is comparable in magnitude to the wave vector of the incoming and scattered photons. In particular, the component along the beam propagation direction is no longer negligible and, consequently, also partial 3D morphological information is imprinted in a single diffraction shot (11, 39). This advantageous feature is, however, counterbalanced by some drawbacks. First, the scattering cross section of the sample material and/or the intensity of the radiation have to be sufficiently high to provide useful scattering signal at high scattering angles (40). When such an experimental condition is met, the extraction of the 3D morphological information from the single diffraction pattern still represents a main challenge. The number of unknowns to be retrieved is much higher than the 2D small-angle case, and a direct extension of the 2D imaging based on phase retrieval algorithms to the 3D case (41) turned out to be not fully reliable (42).

[1]Laboratory for Solid State Physics, ETH Zurich, 8093 Zurich, Switzerland. [2]European XFEL GmbH, 22869 Schenefeld, Germany. [3]Institut für Optik und Atomare Physik, Technische Universität Berlin, 10623 Berlin, Germany. [4]Deutsches Elektronen-Synchrotron DESY, 22607 Hamburg, Germany. [5]Institute of Physics, University of Rostock, 18057 Rostock, Germany. [6]Department of Life, Light and Matter, University of Rostock, 18051 Rostock, Germany. [7]Department of Physics, University of Freiburg, 79104 Freiburg, Germany. [8]Freiburg Materials Research Center, University of Freiburg, 79104 Freiburg, Germany. [9]Max Born Institute, 12489 Berlin, Germany.
*Corresponding author. Email: alcolombo@phys.ethz.ch

To solve this dimensional deficiency, a reduction of the parameters that describe the sample morphology is required. Up to now, wide-angle single-shot diffraction images of single particles have only been reconstructed using strongly constrained candidate geometries (*11*, *13*, *43*) by fitting the experimental data with the simulation. For example, the analysis of the diffraction data of silver nanocrystals presented in (*11*) required the a priori identification of the main crystalline motif of the sample (tetrahedron, octahedron, icosahedron, etc.). Then, the few free parameters of the sample model, like size and orientation, were manually adjusted to fit the simulation as close as possible to the experimental data. Only as a last step, the parameters were fine-tuned automatically. Disadvantages of this procedure are (i) the results are strongly biased by the strictly constrained sample's model, based on the prior knowledge of typical particle geometries, and (ii) already small deviations of the real structures from model shapes prevent a good agreement between measured data and forward simulations, making the search for optimal model parameters more difficult, if not impossible.

Here, we introduce a generic approach to the 3D reconstruction of faceted samples from single-shot wide-angle coherent diffraction patterns, based on a fast simulation method (*44*), a generic model for the sample shapes, and an efficient optimization strategy. We retrieve the 3D shapes of individual silver nanoparticles imaged with FEL pulses at a wavelength of 5.1 nm. Although the fitting approach does not enforce or favor any particle symmetry, regular polyhedra are retrieved in many cases, which were also reported previously (*11*). In addition, combinations of structural motifs and morphologies with partial or broken symmetries arise, as well as agglomerates of silver nanocrystals that were never studied so far due to the lack of suitable imaging tools.

RESULTS

The experimental diffraction data (*43*) are produced by irradiating isolated silver nanoparticles with single FEL pulses at 243 eV (5.1 nm), with pulse duration of 70 fs. Light is recorded up to a maximum of 30° scattering angle, equivalent to a maximum transfer momentum of 0.64 nm^{-1}. The numerical description of the sample was chosen in a way that well accommodates the properties of silver
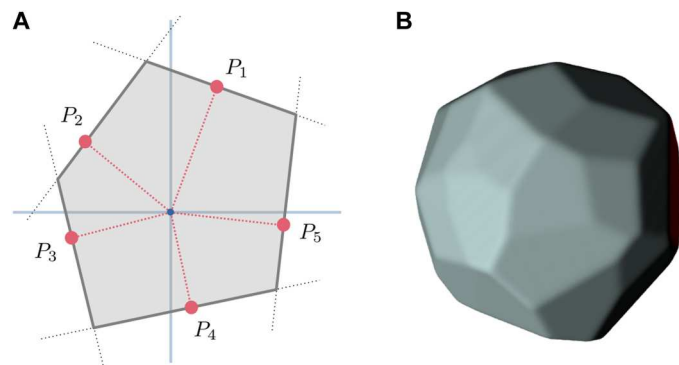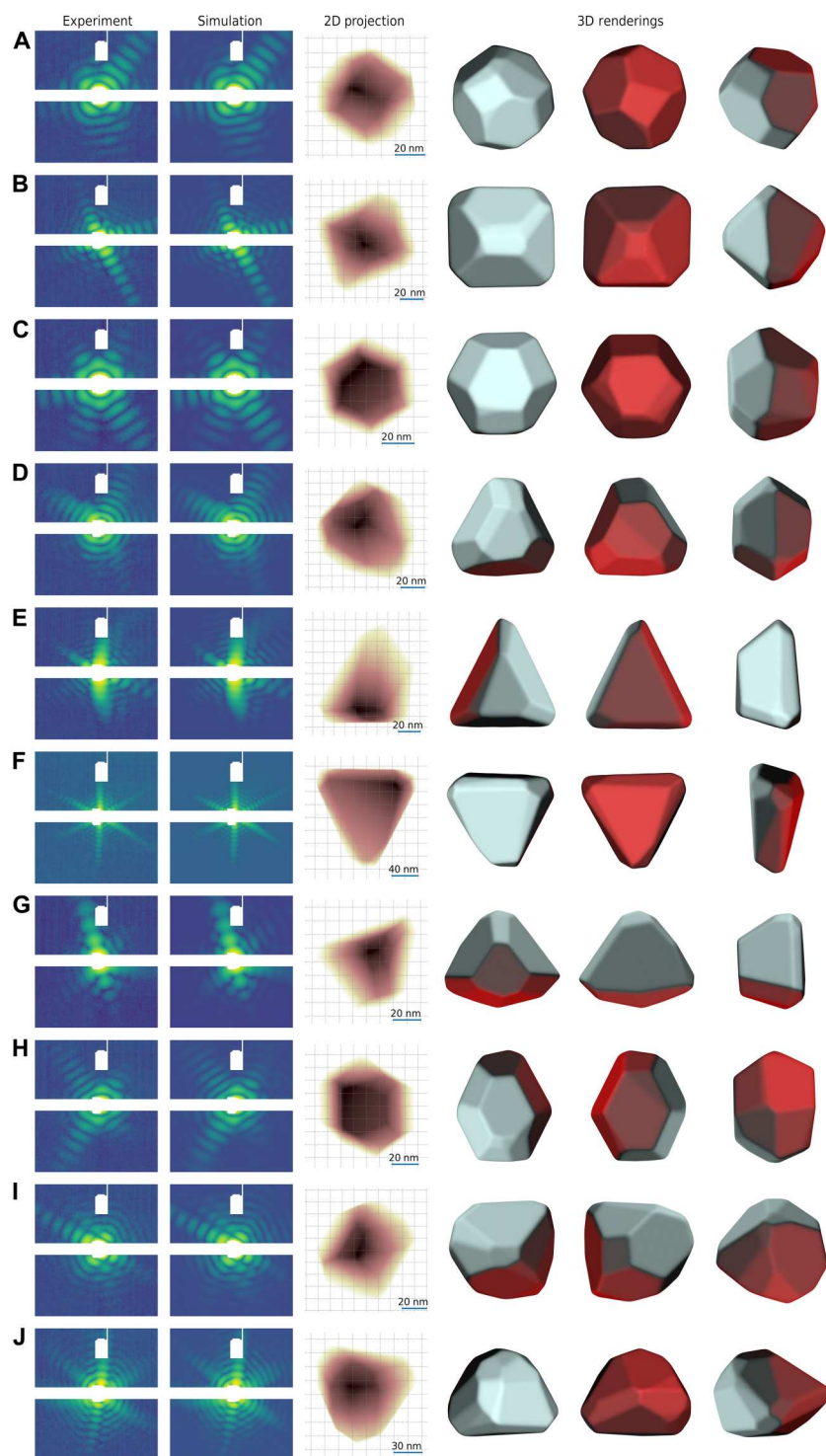
nanoparticles (*11*). The shape is defined by N_p planes, as sketched in Fig. 1A, and is assumed to have a uniform refractive index. The imaging procedure optimizes the plane positions, which are randomly initialized as shown in Fig. 1B, by forward-fitting the experimental diffraction patterns via 3D simulations (*44*). Further details on the experimental data and on the imaging procedure are provided in Materials and Methods.

Imaging of individual nanoparticles

Figure 2 shows a representative subset of the reconstructions for the presented dataset. For each reconstruction, a total of 30 facets were initialized with random positions in space. The first column of Fig. 2 depicts the experimental diffraction pattern, while the second column shows the scattering simulated from the reconstruction, both in logarithmic color scale. The experimental data are given to the fitting routine downscaled and with saturated and missing pixels excluded. The third column shows a 2D projection of the electronic density of the reconstruction onto the detector plane (the plane orthogonal to the beam propagation direction). The last three columns are 3D renderings of the same reconstruction, seen from three different points of view to highlight the main features of the sample. For visualization purposes, the renderings are artificially illuminated with white light from the side that faces the incoming beam, while the opposite side, facing the detector, is lit up in red. We note that the final number of facets in the reconstructions is, in most cases, much lower than 30, as initially given to the fitting routine. The facets that are not required to define the sample morphology are automatically placed by the fitting algorithm in a position that has no effect on the final retrieved shape.

The first examples in Fig. 2 (A to E) depict a selection out of the majority of shapes in our dataset with architectures that can be directly related to known nanoparticle motifs. Truncated octahedra in Fig. 2 (A and B) and twinned truncated tetrahedra in Fig. 2 (C and D) with different truncation positions can be identified. In addition, we find simple truncated tetrahedra with a strongly truncated tip, like the one shown in Fig. 2E, which have not been identified in our previous experiment (*11*). The features in the retrieved structures underline the importance of the specific degree of truncation, which yields different architectures for the same structural motifs. The clear advantage of 3D imaging can be well appreciated by comparing the 2D projections (third column) in Fig. 2 (D and E) with the 3D renderings (last columns). Because of unfortunate orientations, the symmetries of the structures can be barely identified from those 2D projections. As this is the only information that can be derived from iterative phase retrieval (IPR), the examples demonstrate that the structural properties are, in many cases, hardly accessible via small-angle scattering.

The second group of results in Fig. 2 (F to J) are rare or unique examples from the dataset. Figure 2F is a relatively large triangular platelet, which still recalls the triangular motif of the truncated tetrahedron in Fig. 2E. Figure 2G also shows a retrieved nanocrystal that resembles the truncated tetrahedron. However, a small defect is present, visible on the lower side of the renderings, where a main facet is made up of two differently oriented planes. The most pronounced effect is the deformation of the base of the truncated tetrahedron, which is no more a perfectly equilateral triangle. The retrieved architecture in Fig. 2H, which resembles in its main features the shape in Fig. 2C, actually presents two broken symmetries. Here, the twinned tetrahedron is elongated in one direction

Fig. 1. Numerical representation of the sample's morphology. (**A**) 2D sketch of the quantities needed to define the sample's spatial extension. A list of points P_n defines N_p planes, and the space enclosed by those planes defines the sample's shape. (**B**) 3D representation of a shape defined by a random positioning of the facets.

Fig. 2. Fitting results. Each subfigure from (**A**) to (**J**) is made of six columns. The first column is the experimental diffraction pattern (logarithmic color scale). The second is the retrieved diffraction pattern (logarithmic color scale). The third column is a 2D projection of the 3D reconstruction on the plane orthogonal to the beam propagation direction. The last three columns are 3D renderings of the reconstruction result. There, the sample is illuminated with white light from the beam side and with red light from the detector side. For a discussion on the single subfigures, please refer to the main text.

and the truncation level of the tips is different on the two sides. Last, Fig. 2 (I and J) shows examples for strongly asymmetric samples. The sample depicted in Fig. 2I exhibits two different structural motifs. On one side, it resembles an octahedral structure like the one shown in Fig. 2B, while on the opposite side, a large hexagonal facet arises, similarly to the structure shown in Fig. 2H. Instead, it is hard to highlight any symmetry for the reconstruction shown in Fig. 2J, aside from a rough resemblance to a tetrahedral shape similar to Fig. 2 (E and G).

Extension to more complex morphologies

When creating large nanoclusters, the formation of agglomerates (45) is a well-known phenomenon that affects a considerable fraction of the experimental data (8). The presence of silver cluster agglomerates was documented in previous experiments, but the respective diffraction data were excluded from the analysis so far, due to the inability to perform a shape retrieval with the highly constrained models (11). For the analysis of patterns resulting from agglomerates, we allow the presence of multiple convex shapes properly positioned in space in a single shape model. From the numerical point of view, the optimization task becomes highly challenging, as the amount of unknowns to retrieve scales with the amount of crystals, with the addition of the three randomly initialized coordinates that define the relative position of each convex shape. Therefore, we compose each nanoparticle of a total of 30 facets and preset the number of nanocrystals that compose an agglomerate a priori.

A selection of the most interesting reconstructions of agglomerates is shown in Fig. 3. The subfigures are following the scheme of Fig. 2. Figure 3 (A to E) shows agglomerates made of two subclusters, while the reconstructions in Fig. 3 (F to H) are composed of three. We observe, in general, that the structural motifs are clearly identifiable for individual clusters above 50 nm in size. For smaller subclusters, the architecture does not present, in most cases, clear symmetries or motifs, hinting toward a possible stagnation of the optimization procedure in a local optimum, due to a number of possible reasons. First, the scattering signal is dominated by the bigger clusters in the same agglomerate. Second, the crystal itself may not present a clear structure, similar to what is observed for Fig. 2 (I and J). Third, the size of the single facets could be below the actual resolution limit of the diffraction data (see the next section for further discussion). Most of the agglomerates turn out to be composed of individual crystals whose structural motifs were also identified in reconstructions of individual clusters (Fig. 2). However, some cases show peculiar features that raise the need for further discussion. We note that the bigger nanoparticle in Fig. 3B is close to an ideal icosahedron. While this architecture was not identified among the single nanoparticle patterns obtained in our experiment, the shape was repeatedly observed in previous experiments (11). Further, the larger structure in Fig. 3E is peculiar, as it recalls the morphology of a trigonal platelet (see Fig. 2F) with a strong truncation in one direction. The reconstruction shown in Fig. 3H can be considered somewhat surprising. We find an agglomerate of three nanoparticles resembling the shape of a dumbbell, with two small clusters of around 20 nm in size connected by a central column-shaped crystallite, which is the only observation of a more 1D structure in our dataset.

Evaluation of the imaging results

The great variety of structural motifs found in the wide-angle diffraction patterns of large silver nanoclusters, as presented in Figs. 2 and 3, generally agrees well with previous observations (11). In many cases, the observed structural motifs do not correspond to the energetic ground-state structures of silver clusters in this size regime but instead give evidence of a kinematically governed growth process that gets stuck in energy minima of small seed structures in the early phase of growth (11). These meta-stable shapes together with the reconstructed architectures of the agglomerates provide a unique insight into the formation process of metal nanoparticles in the gas phase (45).

We want to underline the fact that the 3D information proves to be crucial for structure determination. In many cases, the retrieved 3D architectures unveil regularities that are neither intuitively expected from rather asymmetric diffraction patterns nor easily discernible from the 2D projection of the sample density, highlighting the huge advantage gained by accessing the third spatial dimension from single diffraction images. We further note that the ability of the approach to retrieve highly regular architectures such as the almost perfect icosahedron in Fig. 3B or the trigonal platelet in Fig. 2E is somewhat striking, as the imaging procedure does not favor any symmetry. The manifestation of these symmetries, which are expected for silver nanocrystals (11), can be considered a strong indication for the quality and appropriateness of our 3D reconstructions. It has to be stressed, nevertheless, that the questions of the reliability and subsequently the resolution of the reconstructions are not yet answered in a generalized way for the 3D case. It has been theoretically shown that a convex morphology has a unique solution (46). This means that only one convex 3D shape exists, giving rise to a single certain 2D wide-angle diffraction pattern. Still, a practical demonstration of the existence of a unique solution to the 3D imaging problem from single shots is lacking even for convex architectures. Furthermore, this possibly safe regime of only convex shapes is clearly left when we attempt the reconstruction of agglomerated particles.

To approach the open questions of uniqueness, reliability, and resolution, in the following we provide two perspectives for discussion by (i) comparing 2D projections from our 3D reconstructions with the 2D densities obtained from well-established IPR using the small-angle part of the diffraction patterns and by (ii) performing a statistical analysis of the convergence properties of the 3D fitting routine.

Comparison with IPR

In Fig. 4, for three exemplary shapes, the 2D density projections from the corresponding 3D structures are compared to 2D reconstructions derived via conventional IPR (47) from only the small-angle part of the patterns (full and restricted small-angle area up to 15° are highlighted on the left of Fig. 4). The results of the two different methods show an excellent agreement within the limited resolution of the IPR, thus strongly confirming the reliability of our results. The resolution of the reconstructed real-space density distribution via IPR is inherently defined by the maximum transferred momentum vector at 15°, leading to a corresponding pixel size of the retrieved 2D projections of 9 nm and to a full-period spatial resolution of 18 nm (48). In contrast, the resolution of the projected 3D shape appears to be much higher, even more than the theoretical limit of the full pattern of 10 nm on the orthogonal plane. In the
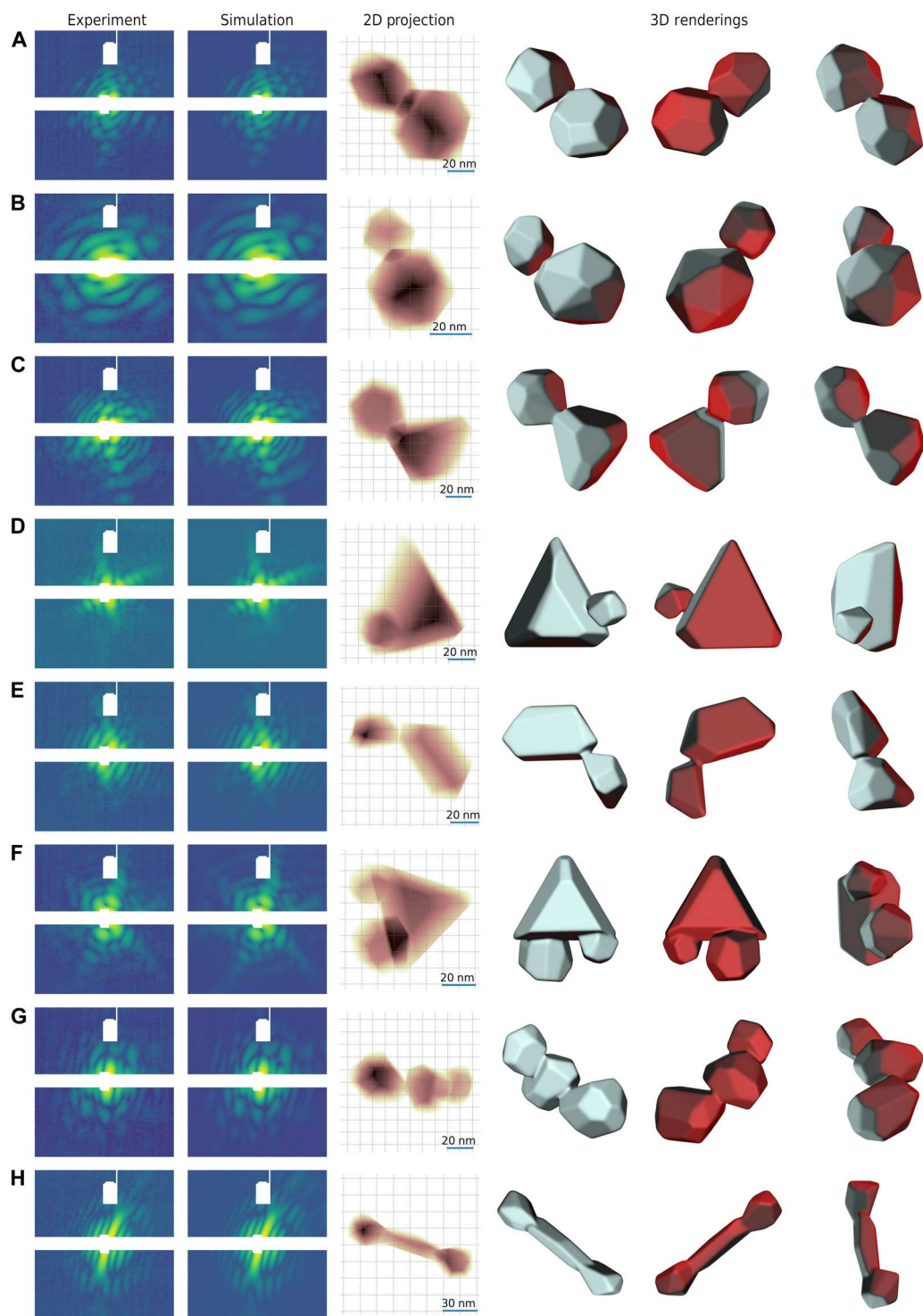
Fig. 3. Fitting results for silver nanocrystal agglomerates. Each subfigure from (**A**) to (**H**) is organized as in Fig. 2.
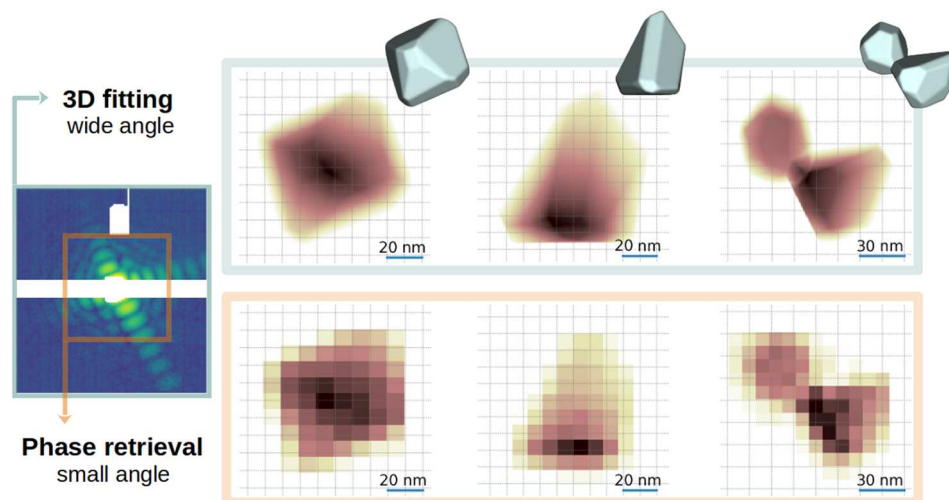
Fig. 4. Comparison of 3D fitting with 2D IPR. The comparison is performed on the experimental data presented in Figs. 2 (B and E) and 3C. The sample diffraction pattern on the left is overlaid by an orange box, which indicates how the diffraction data were cut, to select only small-angle scattering signal on which imaging via phase retrieval algorithms was performed.

following section, we investigate this last aspect, tackling the questions of resolution and consistency of the 3D results from a statistical point of view.

Uniqueness and consistency

To pragmatically test up to which level our results can be considered unique, it is possible to perform a statistical analysis on a set of independent reconstructions of the same diffraction data. In Fig. 5, the results for the same three shapes shown in Fig. 4 are presented. For each structure, 20 independent imaging procedures were carried out, starting from randomly initialized facet coordinates. From the resulting 3D structures, the average density ρ_{avg} was computed. Individual reconstructions are constrained to have sharp edges, i.e., they present a sudden transition between the internal density and the vacuum. However, average density distribution will not exhibit an instantaneous transition from the sample to the vacuum any more, because of the variations between the different independent reconstructions. For each point on the average reconstruction's edge, the transition width is computed, defined as the length of the transition from 10 to 90% of the average density profile along the surface normal. For visualization, the transition width is color-coded onto the structure surface.

Figure 5 is a strong proxy for the stability of the fitting approach in two aspects: The entity of the reconstruction uncertainty is quantified, and we can investigate how this uncertainty is distributed. First, for all three cases, the transition width is much smaller than the cluster size. Second, its spatial distribution strongly varies, depending on not only the structures but also the facet orientations in respect to the FEL beam. For the individual crystals (Fig. 5, A and B), the maximum transition width is observed on those facets oriented perpendicular to the beam. The information about the placement of these facets is mostly encoded by the transfer momenta along the beam propagation direction, and thus encoded in the diffraction signal with a lower resolution.

The same considerations apply for the analysis on the nanocrystal agglomerate in Fig. 5C. Here, in addition, an area of relatively high transition width (and thus uncertainty) is concentrated

around the contact zone of the two nanocrystals. This effect can be explained by two factors. First, the computation of the transition width where the sample's thickness approaches zero is ill-defined. Second, the contact point is in a concavity area: In such a situation, even tiny variations of the position of the facets close to the contact point have a strong effect over the size and positioning of the interface between the two nanoparticles.

Overall, the examples in Fig. 5 reveal up to which detail the fitting result can be trusted, and highlight the degree of uniqueness and stability of the reconstructions. In particular, this analysis reveals uncertainties in the reconstructions that are mostly well below the 10 nm and 36 nm provided by the detected scattering signal on the orthogonal plane and in the depth direction, respectively (see Materials and Methods for further discussion about the resolution).

At a first glance, such a small uncertainty in the reconstructions may lead to the conclusion that the resolution at which structures are resolved is much higher than the one theoretically allowed by the experimental setup. However, this confidence level should not be interpreted as the achieved spatial resolution of our fitting approach, because the presence of constraints introduces a strong bias that prevents a real resolution analysis. As an analog example, the distance of two slits can be inferred from a double-slit experiment to a degree much better than the theoretical resolution limit, while the deviations of the openings from a smooth rectangular shape cannot be determined better than what the resolution limit allows.

DISCUSSION

We have developed a procedure for 3D CDI of faceted nanoparticles using single-shot wide-angle scattering patterns. Our analysis is based on a forward-fitting approach, where a parametrized description of the sample architecture is fitted to the experimental data. The new aspect of our method is the use of a highly generic sample parametrization, which can describe any uniform and convex sample architecture. In contrast to previous works, this
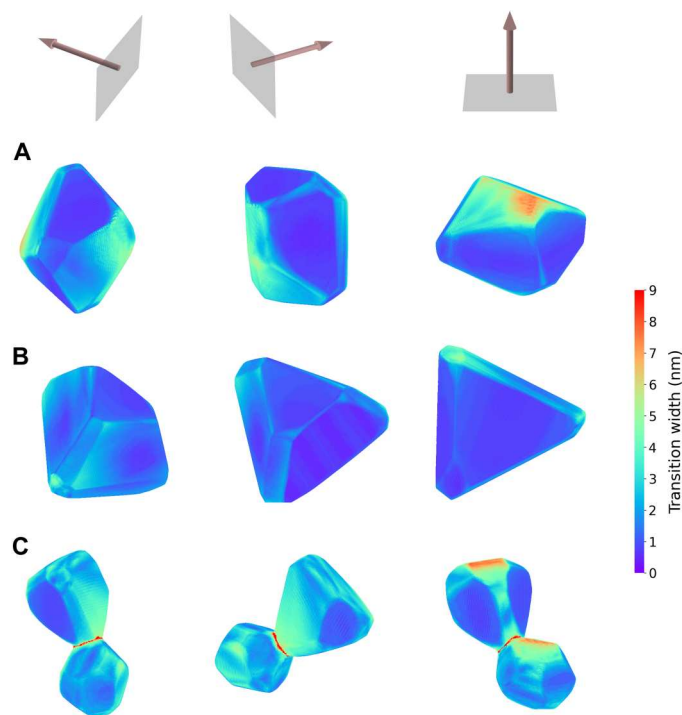
Fig. 5. Analysis of the reconstruction stability. In (**A**) and (**B**), two reconstructed samples of single nanoparticles are shown for three different orientations. These reconstructions are the average of 20 independent fitting procedures. The orientations are indicated by the arrows on the upper row that show the beam propagation direction. For each point on the surface, a transition width is assigned through a colormap, whose scale is indicated on the right. The given value is a measure for the stability of the reconstruction process. In (**C**), the same analysis is presented for a nanocrystal agglomerate.

feature allows to retrieve the morphology of an individual nanoparticle without constraining any symmetry, thus highly reducing the bias toward certain shapes and enormously extending the applicability of the imaging method. The results obtained for silver nanoparticles, imaged at 5.1 nm radiation wavelength, reveal details and geometries compatible with previous experiments, along with architectures that have not been reported so far. The imaging method is extended to the analysis of diffraction patterns from nanocrystal agglomerates, potentially yielding a unique insight into their formation process. Statistical considerations on the reconstructions suggest a confidence level of the results that is well above the spatial resolution theoretically provided by the wide-angle scattering images. Furthermore, the optimization scheme does not depend on the specific parameterization and can, in principle, be extended to any other sample model.

The importance of this work, however, goes well beyond the presented reconstructions. While our demonstration focuses on faceted shapes, the optimization scheme allows for the exploration of different sample parametrizations, which will enable the study of arbitrary, even more complex structures, like complicated agglomerates or heterogenous nanoparticles as well as dynamical processes via time-resolved CDI. Although the actual resolution achieved and the limitations of our imaging approach remain to be fully defined and understood, the results presented here are a clear indication that reliable and quantitative 3D single-particle CDI from single wide-

angle diffraction patterns is possible, at least under the conditions presented. The results of this work open up possibilities for wide-angle CDI that remained unexplored so far and provide an important building block for FEL science toward a real 3D movie of dynamical processes at the nanoscale.

MATERIALS AND METHODS
Experimental data
The experimental data (*43*) treated here were acquired at the CAMP endstation (*49*) of the Free-electron LASer in Hamburg (FLASH) (*50*). Isolated silver nanoparticles of 70 nm average size (equivalent to around 10^7 silver atoms) were produced by a gas aggregation cluster source, based on the Haberland magnetron sputtersource design (*43*, *51*), where large nanocrystals grow by coagulation of small clusters formed in the gas phase from supersaturated metallic vapor. The FEL was tuned to yield a photon energy of 243 eV, equivalent to a wavelength of 5.1 nm, with a pulse duration of around 70 fs. The pulse energy recorded at the CAMP endstation was 30 μJ, corresponding to around 10^{12} photons per pulse, focused to a spot size of 10 μm. The FEL beam intercepted the silver nanoparticles in front of a pn-junction Charge Coupled Device (pnCCD) scattering detector (*52*), composed by two halves with 1024×512 pixel resolution with a pixel size of 75×75 μm. The detector, placed at a distance of 70 mm from the interaction region, was positioned to record scattered light for full 2π azimuth up to 30° scattering angle, equivalent to a maximum transfer momentum of 0.64 nm^{-1}, as shown in Fig. 6.

Spatial resolution and wide angle
The magnitude of the maximum transfer momentum has been calculated via the formula

$$|\overrightarrow{q}_{max}| = |\overrightarrow{k}_0| \cdot 2 \cdot \sin\left(\frac{\theta_{max}}{2}\right) \tag{1}$$

where θ_{max} is the maximum scattering angle recorded by the detector and $|\overrightarrow{k}_0| = \frac{2\pi}{\lambda}$ is the magnitude of the incoming radiation.

As sketched in Fig. 7, in the wide-angle scattering regime, the acquired transfer momentum covers a wide portion of the Ewald sphere, which cannot be approximated as a flat slice in reciprocal space as it is, in contrast, assumed for small-angle scattering experiments. As a consequence, in this experimental condition, the acquired transfer momentum $\overrightarrow{q}$ at high scattering angles has a nonnegligible component in the depth direction (i.e., parallel to the beam propagation axis), which provides low-resolution information about the sample depth.

It is possible to separate the transfer momentum $\overrightarrow{q}$ into the components orthogonal to the beam, $\overrightarrow{q}_\perp$, and parallel to the beam, $\overrightarrow{q}_\parallel$, as depicted in Fig. 7. Their values can be expressed as a function of the scattering angle θ as it follows

$$|\overrightarrow{q}_\perp(\theta)| = |\overrightarrow{k}_0| \sin(\theta)$$
$$|\overrightarrow{q}_\parallel(\theta)| = |\overrightarrow{k}_0| \cdot [1 - \cos(\theta)] \tag{2}$$

The theoretical maximum resolution on the orthogonal plane $\Delta_\perp$ and on the depth axis $\Delta_\parallel$ can be estimated by applying Bragg's
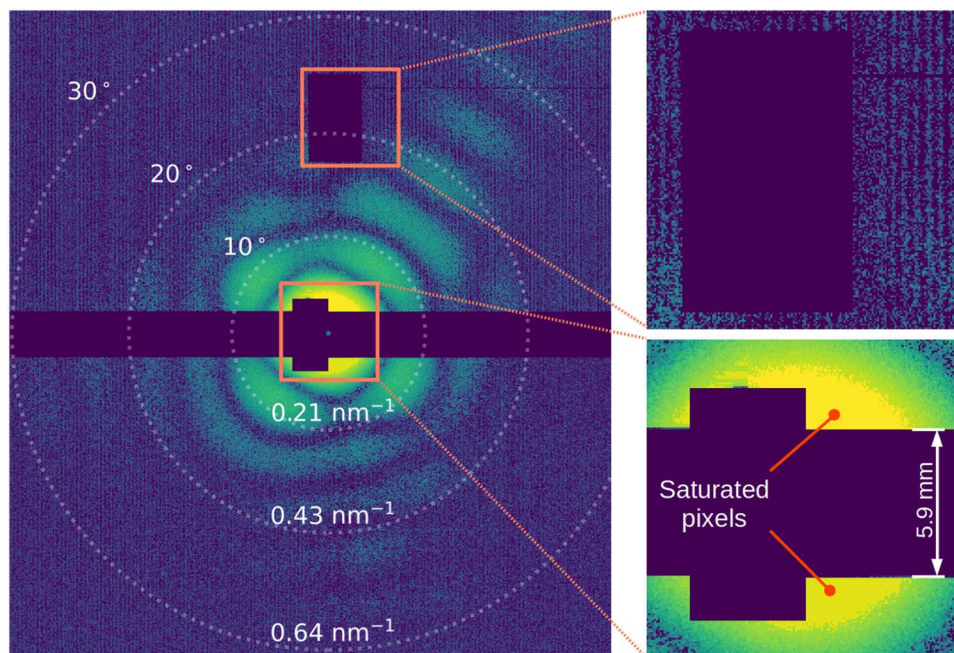
Fig. 6. Example of a scattering pattern. The pattern colormap is in logarithmic scale. Dotted circles indicate the scattering angles on the detector area, for 10°, for 20°, and for 30°. The corresponding values for the transferred momentum $|q|$ are also shown, calculated as indicated in Eq. 1. The upper right inset shows peculiar features of the pnCCD detector, highlighting a rectangular defective area, excluded from the analysis, and noise. In the lower-right inset, pixels where the detector is saturated are shown in yellow. The horizontal blue stripe results from the physical separation of 5.9 mm of the two detector halves. Two notches are visible close to the center: Their role is to reduce the risk of hitting the detector with the main x-ray beam.

law on the two components in Eq. 2. Their values are

$$\Delta_\perp = \frac{2\pi}{|\overrightarrow{q}_\perp(\theta_{max})|} = \frac{\lambda}{\sin(\theta_{max})} \approx 10 \text{ nm}$$

$$\Delta_\parallel = \frac{2\pi}{|\overrightarrow{q}_\parallel(\theta_{max})|} = \frac{\lambda}{1-\cos(\theta_{max})} \approx 38 \text{ nm}$$

(3)

for the experimental conditions treated in this work, where $\theta_{max} \approx 30°$.

The role of the maximum scattering angle is well highlighted by Eq. 3. For example, a 30% reduction in the maximum scattering angle (down to $\approx 20°$) has a marked effect onto $\Delta_\parallel$, which raises up to 85 nm. In such a case, the resolution along the depth is comparable to the cluster size, thus preventing any 3D reconstruction attempt. On the other hand, increasing θ_{max} by 30% to 40° would greatly enhance the depth resolution, almost halving $\Delta_\parallel$ down to 22 nm.

The sample model
The sample's description for this work is conveniently chosen to match the properties of silver nanoparticles (*11*). The shape is formed by N_p planes, as depicted in Fig. 1. Each plane is defined by the coordinates of its point closest to the origin, $P_n = \{x_n, y_n, z_n\}$. In such a way, any plane not containing the origin can be uniquely identified. The volume enclosed by the N_p planes, V_s, defines the sample's spatial extension. The optical properties of the sample are assumed to be uniform within V_s, i.e., the 3D spatial distribution of the refractive index $n(x, y, z)$ has a constant value n_0 in V_s, while it is set to 1 outside. Such a model can describe any sample that (i) does not have concavities, (ii) is homogeneous,

and (iii) has sharp boundaries. While these conditions fit well to the structural properties of silver nanocrystals (*11*), they are ill suited for many other types of morphologies, such as distorted droplets, for which different parametrization basis sets may be chosen, e.g., expansion in spherical harmonics as described in (*44*). For further considerations about the sample model, see the Supplementary Materials.

The total number of facets involved in the fitting procedure must be, at least, equal to the amount of faces that can fully describe the sample shape. Their number is dependent on the cluster morphology and can be as low as 14 for the truncated tetrahedron in Fig. 2E (including the tip and edge truncation). However, using the lowest possible amount of facets for the fitting would require a priori knowledge on the cluster architecture, thus making the imaging approach less generic. On the other side, the number of facets cannot indefinitely be increased mainly due to computational constraints as the reconstruction time scales at least linearly with the amount of free parameters involved. For these reasons, the same amount of facets was considered for all the reconstructions presented here to reduce the a priori bias of the imaging method. By setting the number of facets to 30, the computation time was kept manageable while at the same time all optimized shapes revealed less than 30 shape-defining facets.

The optimization task
Our imaging approach is based on the so-called forward fitting, where the free parameters are tuned to optimize the similarity between the simulated and the experimental pattern. The latter is downscaled through an 8 × 8 pixel binning, to speed up the simulation time (*44*) without having impact on the reconstruction
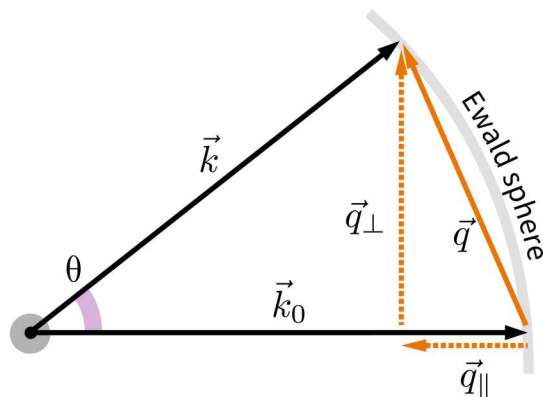
Fig. 7. Geometrical representation of the transfer momentum. In the wide-angle scattering regime, the depth component $\vec{q}_{\parallel}$ of the transfer momentum $\vec{q}$ is not negligible at high scattering angles.

quality, as long as the oversampling condition is met (*26, 53*). In our case, the similarity is encoded in the optimization target, which has to be minimized via a suitable algorithm. Given I_{ij}^{exp} the matrix that contains the intensity values of the experimental diffraction pattern, the optimization target E is defined as

$$E(\vec{p}) = \sum_{i,j} |I_{ij}^{exp} - I_{ij}^{sim}(\vec{p})| \qquad (4)$$

This equation defines the metric used to calculate the distance between the simulated pattern I^{sim} and the experimental one I^{exp}. I^{sim} and, consequently, the target E are functions of the vector $\vec{p}$, which contains all the parameters that are subject to the

Fig. 8. Flowchart of the optimization strategy used for imaging. For a step-by-step description, see the main text.

optimization procedure. First, $\vec{p}$ contains the $3N_p$ coordinates of the N_p planes. In addition, it encodes the complex refractive index n, expressed as $1 - \delta + i\beta$, where δ and β are allowed to assume values in the range of $\pm30\%$ of their tabulated value of 0.01 and 0.003, respectively (*54*). Last, $\vec{p}$ includes four additional numbers: two of them are the x and y coordinates of the center of the diffraction pattern (which can vary by up to ±2 pixels from shot to shot due to slightly different pointing directions of the FEL), one is a global offset value in the diffraction data (to account for white background noise of the pnCCD detector), and the last is a normalization factor.

For the analysis of cluster agglomerates, a number N_s of faceted shapes are considered. Each of the N_s shapes has its own set of facets and refractive index. Furthermore, each additional shape requires the three spatial coordinates for its relative positioning. Thus, the total amount of free parameters N_f involved in the fitting can be expressed by the following formula

$$N_f = (3N_p + 2) \cdot N_s + 3 \cdot (N_s - 1) + 4 \qquad (5)$$

For individual nanocrystals ($N_s = 1$) imaged with 30 facets ($N_p = 30$), the number of parameters involved in the optimization is $N_f = 96$. This number raises up to 191 and 286 for agglomerates composed by two and three subcrystals, respectively.

The scope of the imaging procedure is to find the parameters $\vec{p}$ that fit best the experimental data I^{exp}. The solution to the imaging problem $\vec{p}^{sol}$ can be defined as the solution of an optimization task

$$\vec{p}^{sol} = \{\vec{p}: E[\vec{p}] < E[\vec{p'}] \,\forall\, \vec{p'} \neq \vec{p}\} \qquad (6)$$

where E is the optimization target defined in Eq. 4.

Any optimization strategy requires several evaluations of the optimization target, each of which implies a full wide-angle scattering simulation. Because of the relatively small variation from unity of the silver's refractive index at 243 eV, the simulated pattern I^{sim} as a function of parameter $\vec{p}$ can be obtained through a fast approximate simulation method, called Scatman (*44*), capable of providing a simulated pattern in few milliseconds. Nevertheless, the optimization of $E(\vec{p})$ is highly challenging, due to the high amount of free parameters involved and the still relevant computational cost of the error evaluation. For these reasons, an ad hoc optimization strategy was developed for this work, and it is described in the following section.

The fitting routine

The optimization strategy used in this work belongs to the family of Memetic Algorithms (*55, 56*). These algorithms merge stochastic and deterministic optimization techniques, aiming at combining their strengths. In particular, a differential genetic algorithm (*57*) is combined with a simplex-based Nelder-Mead algorithm (*58*). In this section, we give a description of the algorithm structure, following the flowchart in Fig. 8.

The Initialization step initializes a population P of candidate solutions. In particular, for each element P_i, a random value d is extracted. Then, the N_p facets are randomly placed in space, all at the same distance d. The reason for this choice is to ensure that, at the starting point, all the facets have an effect in determining the nanocluster morphology. For the present work, the size of the population P was set to 16,000.
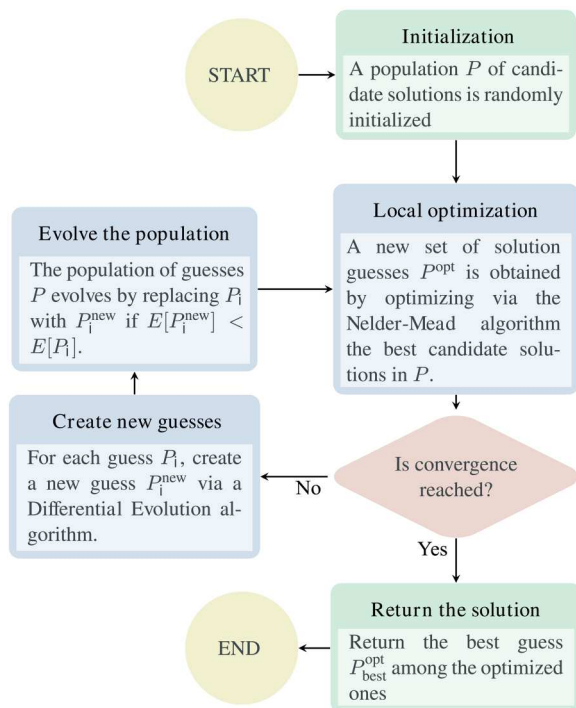
The Local optimization step involves a local optimization of the free parameters. Here, the term local is used because the aim of this step is to reach a close local optimum of the optimization target. This is achieved via a simplex search algorithm (58). For this step, the total number of target function evaluations was set to $30 \times N_f$, where N_f is the amount of free parameters involved in the optimization (see the previous section). In case of single nanoclusters, this is equivalent to 2280. Because of the huge computational cost of this step, the local optimization cannot be performed on all the candidate solutions in P, but only on the 16 with the lowest error. The set of locally optimized shapes is here addressed as P^{opt}.

The following two steps, Create new guesses and Evolve the population, are inherited from the differential evolution optimization strategy (57) and aim at a global exploration of the parameter space. In the first part, for each element P_i, a new candidate solution P_i^{new} is built by merging the parameters of P_i with other three candidates. The first of these three is randomly chosen among the locally optimized population P^{opt}, while the other two are randomly selected from the whole population P. Last, each of the newly formed candidate solutions P_i^{new} is compared with P_i. If the error of the new one is lower, P_i is replaced by P_i^{new}.

A full cycle of the algorithm's main loop as shown in Fig. 8 can be broadly referred to as a generation, following the terminology often used for genetic algorithms. The stopping criterion of the imaging algorithm can be based on its convergence status, which can be, for example, evaluated by looking at the entity of the parameters' differences within the population P. However, for this work, we considered safer to use the total amount of generations as a stopping condition, set here to 200. The final result yielded by the algorithm is the best candidate solution among the optimized ones P^{opt} in the last generation.

An intuitive visualization of the reconstruction procedure is provided by the movies in the Supplementary Materials. For the full technical details, please refer to the imaging software released online as open-source (https://gitlab.ethz.ch/nux/numerical-physics/3d-imaging).

Limitations
The imaging approach presented here comes with some limitations. In this section, we summarize them to provide a better overview to the reader and to encourage the development of the imaging method. The first restriction concerns the simulation method. Exact simulations that solve Maxwell's equations numerically, e.g., via the finite-difference time-domain (FDTD) method (59, 60), have a computational cost that makes them incompatible with a forward-fitting approach, as each evaluation of the optimization target involves a full simulation of a wide-angle scattering pattern. It is thus necessary to rely on an approximate method, in our case, the Scatman (44), which delivers a full simulation within few milliseconds. Its main drawback is that results deviate from the exact solution if the material's refractive index is far from 1 and/or the simulated sample is too large. For an exhaustive discussion on the simulation method and its constraints, please see (44). Despite the use of a fast simulation tool, the whole fitting procedure still requires approximately an hour for reaching convergence. This means that, at the current stage, the method is hardly applicable to more than a few hundreds of diffraction patterns.

The second restriction is still connected to the material optical properties. Scattered light has to be recorded at high scattering angles to provide 3D information. However, it is not always possible to collect sufficient light at wide angles due to the typically low scattering cross sections in the x-ray regime. On the other hand, the absorption cross section must not be too high: A sufficient amount of light needs to reach the full sample to provide enough scattering at all depths. However, this problem is being mitigated by the recent developments of x-ray free electron lasers. There, pulse energies of several millijoules can be delivered at photon energies with low absorption cross section and focused to very high intensities, thus providing meaningful signal at high scattering angles.

A third class of limitations directly derives from the shape model. The faceted description of the sample restricts the analysis to samples that are convex and uniform and have sharp edges. This kind of samples is only a small subset of the nanostructures that are actually of interest for the scientific community. Extensions of the method to different shape representations, which allow more complex structures, are currently under study, and their reliability has to be investigated.

Supplementary Materials
This PDF file includes:
Edge Analysis
The role of constraints
Figs. S1 and S2
Legends for movies S1 and S2

Other Supplementary Material for this manuscript includes the following:
Movies S1 and S2

REFERENCES AND NOTES
1. J. Miao, P. Charalambous, J. Kirz, D. Sayre, Extending the methodology of x-ray crystallography to allow imaging of micrometre-sized non-crystalline specimens. *Nature* **400**, 342–344 (1999).
2. H. N. Chapman, K. A. Nugent, Coherent lensless X-ray imaging. *Nat. Photonics* **4**, 833–839 (2010).
3. J. Miao, R. L. Sandberg, C. Song, Coherent X-ray diffraction imaging. *IEEE J. Sel. Top. Quantum Electron.* **18**, 399–410 (2012).
4. M. M. Seibert, T. Ekeberg, F. R. N. C. Maia, M. Svenda, J. Andreasson, O. Jönsson, D. Odić, B. Iwan, A. Rocker, D. Westphal, M. Hantke, D. P. DePonte, A. Barty, J. Schulz, L. Gumprecht, N. Coppola, A. Aquila, M. Liang, T. A. White, A. Martin, C. Caleman, S. Stern, C. Abergel, V. Seltzer, J.-M. Claverie, C. Bostedt, J. D. Bozek, S. Boutet, A. A. Miahnahri, M. Messerschmidt, J. Krzywinski, G. Williams, K. O. Hodgson, M. J. Bogan, C. Y. Hampton, R. G. Sierra, D. Starodub, I. Andersson, S. Bajt, M. Barthelmess, J. C. H. Spence, P. Fromme, U. Weierstall, R. Kirian, M. Hunter, R. B. Doak, S. Marchesini, S. P. Hau-Riege, M. Frank, R. L. Shoeman, L. Lomb, S. W. Epp, R. Hartmann, D. Rolles, A. Rudenko, C. Schmidt, L. Foucar, N. Kimmel, P. Holl, B. Rudek, B. Erk, A. Hömke, C. Reich, D. Pietschner, G. Weidenspointner, L. Strüder, G. Hauser, H. Gorke, J. Ullrich, I. Schlichting, S. Herrmann, G. Schaller, F. Schopper, H. Soltau, K.-U. Kühnel, R. Andritschke, C.-D. Schröter, F. Krasniqi, M. Bott, S. Schorb, D. Rupp, M. Adolph, T. Gorkhover, H. Hirsemann, G. Potdevin, H. Graafsma, B. Nilsson, H. N. Chapman, J. Hajdu, Single mimivirus particles intercepted and imaged with an x-ray laser. *Nature* **470**, 78–81 (2011).
5. Z. Sun, A. Al Haddad, S. Augustin, G. Knopp, J. Knurr, K. Schnorr, C. Bostedt, Ultrafast single-particle imaging with intense x-ray pulses. *Chimia* **76**, 529 (2022).
6. 4T. Ekeberg, M. Svenda, C. Abergel, F. R. N. C. Maia, V. Seltzer, J.-M. Claverie, M. Hantke, O. Jönsson, C. Nettelblad, G. van der Schot, M. Liang, D. P. DePonte, A. Barty, M. M. Seibert, B. Iwan, I. Andersson, N. D. Loh, A. V. Martin, H. Chapman, C. Bostedt, J. D. Bozek, K. R. Ferguson, J. Krzywinski, S. W. Epp, D. Rolles, A. Rudenko, R. Hartmann, N. Kimmel, J. Hajdu, Three-dimensional reconstruction of the giant mimivirus particle with an x-ray free-electron laser. *Phys. Rev. Lett.* **114**, 098102 (2015).

7. T. Ekeberg, D. Assalauova, J. Bielecki, R. Boll, B. J. Daurer, L. A. Eichacker, L. E. Franken, D. E. Galli, L. Gelisio, L. Gumprecht, L. H. Gunn, J. Hajdu, R. Hartmann, D. Hasse, A. Ignatenko, J. Koliyadu, O. Kulyk, R. Kurta, M. Kuster, W. Lugmayr, J. Lübke, A. P. Mancuso, T. Mazza, C. Nettelblad, Y. Ovcharenko, D. E. Rivas, A. K. Samanta, P. Schmidt, E. Sobolev, N. Timneanu, S. Usenko, D. Westphal, T. Wollweber, L. Worbs, P. L. Xavier, H. Yousef, K. Ayyer, H. N. Chapman, J. A. Sellberg, C. Seuring, I. A. Vartanyants, J. Küpper, M. Meyer, F. R. N. C. Maia, Observation of a single protein by ultrafast X-ray diffraction. bioRxiv 2022. 03.09.483477 [Preprint]. 2 November 2022.https://doi.org/10.1101/2022.03.09.483477.

8. D. Rupp, M. Adolph, T. Gorkhover, S. Schorb, D. Wolter, R. Hartmann, N. Kimmel, C. Reich, T. Feigl, A. R. de Castro, R. Treusch, L. Stüder, T. Möller, C. Bostedt, Identification of twinned gas phase clusters by single-shot scattering with intense soft x-ray pulses. New J. Phys. 14, 055016 (2012).

9. A. Niozu, Y. Kumagai, T. N. Hiraki, H. Fukuzawa, K. Motomura, M. Bucher, K. Asa, Y. Sato, Y. Ito, D. You, T. Ono, Y. Li, E. Kukk, C. Miron, L. Neagu, C. Callegari, M. D. Fraia, G. Rossi, D. E. Galli, T. Pincelli, A. Colombo, S. Owada, K. Tono, T. Kameshima, Y. Joti, T. Katayama, T. Togashi, M. Yabashi, K. Matsuda, C. Bostedt, K. Ueda, K. Nagaya, Crystallization kinetics of atomic crystals revealed by a single-shot and single-particle x-ray diffraction experiment. Proc. Natl. Acad. Sci. U.S.A. 118, e2111747118 (2021).

10. T. Gorkhover, A. Ulmer, K. Ferguson, M. Bucher, F. R. N. C. Maia, J. Bielecki, T. Ekeberg, M. F. Hantke, B. J. Daurer, C. Nettelblad, J. Andreasson, A. Barty, P. Bruza, S. Carron, D. Hasse, J. Krzywinski, D. S. D. Larsson, A. Morgan, K. Mühlig, M. Müller, K. Okamoto, A. Pietrini, D. Rupp, M. Sauppe, G. van der Schot, M. Seibert, J. A. Sellberg, M. Svenda, M. Swiggers, N. Timneanu, D. Westphal, G. Williams, A. Zani, H. N. Chapman, G. Faigel, T. Möller, J. Hajdu, C. Bostedt, Femtosecond X-ray fourier holography imaging of free-flying nanoparticles. Nat. Photonics 12, 150–153 (2018).

11. I. Barke, H. Hartmann, D. Rupp, L. Flückiger, M. Sauppe, M. Adolph, S. Schorb, C. Bostedt, R. Treusch, C. Peltz, S. Bartling, T. Fennel, K.-H. Meiwes-Broer, T. Möller, The 3D-architecture of individual free silver nanoparticles captured by X-ray scattering. Nat. Commun. 6, 6187 (2015).

12. M. Bogan, S. Boutet, H. N. Chapman, S. Marchesini, A. Barty, W. H. Benner, U. Rohner, M. Frank, S. P. Hau-Riege, S. Bajt, B. Woods, M. M. Seibert, B. Iwan, N. Timneanu, J. Hajdu, J. Schulz, Aerosol imaging with a soft X-ray free electron laser. Aerosol Sci. Tech. 44, 1–6 (2010).

13. B. Langbehn, K. Sander, Y. Ovcharenko, C. Peltz, A. Clark, M. Coreno, R. Cucini, M. Drabbels, P. Finetti, M. Di Fraia, L. Giannessi, C. Grazioli, D. Iablonskyi, A. C. LaForge, T. Nishiyama, V. O. Álvarez de Lara, P. Piseri, O. Plekan, K. Ueda, J. Zimmermann, K. C. Prince, F. Stienkemeier, C. Callegari, T. Fennel, D. Rupp, T. Möller, Three-dimensional shapes of spinning helium nanodroplets. Phys. Rev. Lett. 121, 255301 (2018).

14. A. J. Feinberg, F. Laimer, R. M. P. Tanyag, B. Senfftleben, Y. Ovcharenko, S. Dold, M. Gatchell, S. M. O. O'Connell-Lopez, S. Erukala, C. A. Saladrigas, B. W. Toulson, A. Hoffmann, B. Kamerin, R. Boll, A. De Fanis, P. Grychtol, T. Mazza, J. Montano, K. Setoodehnia, D. Lomidze, R. Hartmann, P. Schmidt, A. Ulmer, A. Colombo, M. Meyer, T. Möller, D. Rupp, O. Gessner, P. Scheier, A. F. Vilesov, X-ray diffractive imaging of highly ionized helium nanodroplets. Phys. Rev. Res. 4, L022063 (2022).

15. C. Bostedt, E. Eremina, D. Rupp, M. Adolph, H. Thomas, M. Hoener, A. R. de Castro, J. Tiggesbäumker, K.-H. Meiwes-Broer, T. Laarmann, H. Wabnitz, E. Plönjes, R. Treusch, J. R. Schneider, T. Möller, Ultrafast X-ray scattering of xenon nanoparticles: Imaging transient states of matter. Phys. Rev. Lett. 108, 093401 (2012).

16. L. Flückiger, D. Rupp, M. Adolph, T. Gorkhover, M. Krikunova, M. Müller, T. Oelze, Y. Ovcharenko, M. Sauppe, S. Schorb, C. Bostedt, S. Düsterer, M. Harmand, H. Redlin, R. Treusch, T. Möller, Time-resolved x-ray imaging of a laser-induced nanoplasma and its neutral residuals. New J. Phys. 18, 043017 (2016).

17. Y. Ihm, D. H. Cho, D. Sung, D. Nam, C. Jung, T. Sato, S. Kim, J. Park, S. Kim, M. Gallagher-Jones, Y. Kim, R. Xu, S. Owada, J. H. Shim, K. Tono, M. Yabashi, T. Ishikawa, J. Miao, D. Y. Noh, C. Song, Direct observation of picosecond melting and disintegration of metallic nanoparticles. Nat. Commun. 10, 2411 (2019).

18. D. Rupp, L. Flückiger, M. Adolph, A. Colombo, T. Gorkhover, M. Harmand, M. Krikunova, J. P. Müller, T. Oelze, Y. Ovcharenko, M. Richter, M. Sauppe, S. Schorb, R. Treusch, D. Wolter, C. Bostedt, T. Möller, Imaging plasma formation in isolated nanoparticles with ultrafast resonant scattering. Struct. Dyn. 7, 034303 (2020).

19. C. Peltz, J. A. Powell, P. Rupp, A. Summers, T. Gorkhover, M. Gallei, I. Halfpap, E. Antonsson, B. Langer, C. Trallero-Herrero, C. Graf, D. Ray, Q. Liu, T. Osipov, M. Bucher, K. Ferguson, S. Möller, S. Zherebtsov, D. Rolles, E. Rühl, G. Coslovich, R. N. Coffee, C. Bostedt, A. Rudenko, M. F. Kling, T. Fennel, Few-femtosecond resolved imaging of laser-driven nanoplasma expansion. New J. Phys. 24, 043024 (2022).

20. C. Jung, Y. Ihm, D. H. Cho, H. Lee, D. Nam, S. Kim, I.-T. Eom, J. Park, C. Kim, Y. Kim, J. Fan, N. Ji, J. R. Morris, S. Owada, K. Tono, J. H. Shim, H. Jiang, M. Yabashi, T. Ishikawa, D. Y. Noh, C. Song, Inducing thermodynamically blocked atomic ordering via strongly driven nonequilibrium kinetics. Sci. Adv. 7, eabj8552 (2021).

21. T. Gorkhover, S. Schorb, R. Coffee, M. Adolph, L. Foucar, D. Rupp, A. Aquila, J. D. Bozek, S. W. Epp, B. Erk, L. Gumprecht, L. Holmegaard, A. Hartmann, R. Hartmann, G. Hauser, P. Holl, A. Hömke, P. Johnsson, N. Kimmel, K.-U. Kühnel, M. Messerschmidt, C. Reich, A. Rouzée, B. Rudek, C. Schmidt, J. Schulz, H. Soltau, S. Stern, G. Weidenspointner, B. White, J. Küpper, L. Strüder, I. Schlichting, J. Ullrich, D. Rolles, A. Rudenko, T. Möller, C. Bostedt, Femtosecond and nanometre visualization of structural dynamics in superheated nanoparticles. Nat. Photonics 10, 93–97 (2016).

22. T. Nishiyama, Y. Kumagai, A. Niozu, H. Fukuzawa, K. Motomura, M. Bucher, Y. Ito, T. Takanashi, K. Asa, Y. Sato, D. You, Y. Li, T. Ono, E. Kukk, C. Miron, L. Neagu, C. Callegari, M. Di Fraia, G. Rossi, D. E. Galli, T. Pincelli, A. Colombo, T. Kameshima, Y. Joti, T. Hatsui, S. Owada, T. Katayama, T. Togashi, K. Tono, M. Yabashi, K. Matsuda, C. Bostedt, K. Nagaya, K. Ueda, Ultrafast structural dynamics of nanoparticles in intense laser fields. Phys. Rev. Lett. 123, 123201 (2019).

23. B. Langbehn, Y. Ovcharenko, A. Clark, M. Coreno, R. Cucini, A. Demidovich, M. Drabbels, P. Finetti, M. D. Fraia, L. Giannessi, C. Grazioli, D. Iablonskyi, A. C. LaForge, T. Nishiyama, V. O. Álvarez de Lara, C. Peltz, P. Piseri, O. Plekan, K. Sander, K. Ueda, T. Fennel, K. C. Prince, F. Stienkemeier, C. Callegari, T. Möller, D. Rupp, Diffraction imaging of light induced dynamics in xenon-doped helium nanodroplets. New J. Phys. 24, 113043 (2022).

24. M. Mudrich, A. LaForge, A. Ciavardini, P. O'Keeffe, C. Callegari, M. Coreno, A. Demidovich, M. Devetta, M. D. Fraia, M. Drabbels, P. Finetti, O. Gessner, C. Grazioli, A. Hernando, D. M. Neumark, Y. Ovcharenko, P. Piseri, O. Plekan, K. Prince, R. Richter, M. P. Ziemkiewicz, T. Möller, J. Eloranta, M. Pi, M. Barranco, F. Stienkemeier, Ultrafast relaxation of photoexcited superfluid He nanodroplets. Nat. Commun. 11, 112 (2020).

25. A. Guinier, G. Fournet, C. Walker, G. H. Vineyard, Small-angle scattering of X-rays. Phys. Today 9, 38–39 (1956).

26. D. Sayre, Some implications of a theorem due to Shannon. Acta Crystallogr. 5, 843 (1952).

27. J. R. Fienup, Phase retrieval algorithms: A comparison. Appl. Optics 21, 2758–2769 (1982).

28. S. Marchesini, H. He, H. N. Chapman, S. P. Hau-Riege, A. Noy, M. R. Howells, U. Weierstall, J. C. Spence, X-ray image reconstruction from a diffraction pattern alone. Phys. Rev. B 68, 140101 (2003).

29. N. D. Loh, C. Y. Hampton, A. V. Martin, D. Starodub, R. G. Sierra, A. Barty, A. Aquila, J. Schulz, L. Lomb, J. Steinbrener, R. L. Shoeman, S. Kassemeyer, C. Bostedt, J. Bozek, S. W. Epp, B. Erk, R. Hartmann, D. Rolles, A. Rudenko, B. Rudek, L. Foucar, N. Kimmel, G. Weidenspointner, G. Hauser, P. Holl, E. Pedersoli, M. Liang, M. S. Hunter, L. Gumprecht, N. Coppola, C. Wunderer, H. Graafsma, F. R. N. C. Maia, T. Ekeberg, M. Hantke, H. Fleckenstein, H. Hirsemann, K. Nass, T. A. White, H. J. Tobias, G. R. Farquar, W. H. Benner, S. P. Hau-Riege, C. Reich, A. Hartmann, H. Soltau, S. Marchesini, S. Bajt, M. Barthelmess, P. Bucksbaum, K. O. Hodgson, L. Strüder, J. Ullrich, M. Frank, I. Schlichting, H. N. Chapman, M. J. Bogan, Fractal morphology, imaging and mass spectrometry of single aerosol particles in flight. Nature 486, 513–517 (2012).

30. E. Pedersoli, N. D. Loh, F. Capotondi, C. Y. Hampton, R. G. Sierra, D. Starodub, C. Bostedt, J. Bozek, A. J. Nelson, M. Aslam, S. Li, V. P. Dravid, A. V. Martin, A. Aquila, A. Barty, H. Fleckenstein, L. Gumprecht, M. Liang, K. Nass, J. Schulz, T. A. White, N. Coppola, S. Bajt, M. Barthelmess, H. Graafsma, H. Hirsemann, C. Wunderer, S. W. Epp, B. Erk, B. Rudek, A. Rudenko, L. Foucar, S. Kassemeyer, L. Lomb, D. Rolles, R. L. Shoeman, J. Steinbrener, R. Hartmann, A. Hartmann, G. Hauser, P. Holl, N. Kimmel, C. Reich, H. Soltau, G. Weidenspointner, W. H. Benner, G. R. Farquar, S. P. Hau-Riege, M. S. Hunter, T. Ekeberg, M. Hantke, F. R. N. C. Maia, H. J. Tobias, S. Marchesini, M. Frank, L. Strüder, I. Schlichting, J. Ullrich, H. N. Chapman, P. H. Bucksbaum, M. Kiskinova, M. J. Bogan, Mesoscale morphology of airborne core-shell nanoparticle clusters: X-ray laser coherent diffraction imaging. J. Phys. B 46, 164033 (2013).

31. J. Miao, C.-C. Chen, C. Song, Y. Nishino, Y. Kohmura, T. Ishikawa, D. Ramunno-Johnson, T.-K. Lee, S. H. Risbud, Three-dimensional GaN−Ga₂O₃ core shell structure revealed by X-ray diffraction microscopy. Phys. Rev. Lett. 97, 215503 (2006).

32. H. Jiang, C. Song, C.-C. Chen, R. Xu, K. S. Raines, B. P. Fahimian, C.-H. Lu, T.-K. Lee, A. Nakashima, J. Urano, T. Ishikawa, F. Tamanoi, J. Miao, Quantitative 3D imaging of whole, unstained cells by using X-ray diffraction microscopy. Proc. Natl. Acad. Sci. U.S.A. 107, 11234–11239 (2010).

33. I. V. Lundholm, J. A. Sellberg, T. Ekeberg, M. F. Hantke, K. Okamoto, G. van der Schot, J. Andreasson, A. Barty, J. Bielecki, P. Bruza, M. Bucher, S. Carron, B. J. Daurer, K. Ferguson, D. Hasse, J. Krzywinski, D. S. D. Larsson, A. Morgan, K. Mühlig, M. Müller, C. Nettelblad, A. Pietrini, H. K. N. Reddy, D. Rupp, M. Sauppe, M. Seibert, M. Svenda, M. Swiggers, N. Timneanu, A. Ulmer, D. Westphal, G. Williams, A. Zani, G. Faigel, H. N. Chapman, T. Möller, C. Bostedt, J. Hajdu, T. Gorkhover, F. R. N. C. Maia, Considerations for three-dimensional image reconstruction from experimental data in coherent diffractive imaging. IUCrJ 5, 531–541 (2018).

34. N. D. Loh, M. J. Bogan, V. Elser, A. Barty, S. Boutet, S. Bajt, J. Hajdu, T. Ekeberg, F. R. N. C. Maia, J. Schulz, M. M. Seibert, B. Iwan, N. Timneanu, S. Marchesini, I. Schlichting, R. L. Shoeman, L. Lomb, M. Frank, M. Liang, H. N. Chapman, Cryptotomography: Reconstructing 3D fourier

intensities from randomly oriented single-shot diffraction patterns. *Phys. Rev. Lett.* **104**, 225501 (2010).

35. D. H. Cho, Z. Shen, Y. Ihm, D. H. Wi, C. Jung, D. Nam, S. Kim, S.-Y. Park, K. S. Kim, D. Sung, H. Lee, J.-Y. Shin, J. Hwang, S. Y. Lee, S. Y. Lee, S. W. Han, D. Y. Noh, N. D. Loh, C. Song, High-throughput 3d ensemble characterization of individual core–shell nanoparticles with x-ray free electron laser single-particle imaging. *ACS Nano* **15**, 4066–4076 (2021).

36. N.-T. D. Loh, V. Elser, Reconstruction algorithm for single-particle diffraction imaging experiments. *Phys. Rev. E* **80**, 026705 (2009).

37. R. Xu, H. Jiang, C. Song, J. A. Rodriguez, Z. Huang, C.-C. Chen, D. Nam, J. Park, M. Gallagher-Jones, S. Kim, S. Kim, A. Suzuki, Y. Takayama, T. Oroguchi, Y. Takahashi, J. Fan, Y. Zou, T. Hatsui, Y. Inubushi, T. Kameshima, K. Yonekura, T. Tono, T. Togashi, T. Sato, M. Yamamoto, M. Nakasako, M. Yabashi, T. Ishikawa, J. Miao, Single-shot three-dimensional structure determination of nanocrystals with femtosecond X-ray free-electron laser pulses. *Nat. Commun.* **5**, 4061 (2014).

38. K. Ayyer, P. L. Xavier, J. Bielecki, Z. Shen, B. J. Daurer, A. K. Samanta, S. Awel, R. Bean, A. Barty, M. Bergemann, T. Ekeberg, A. D. Estillore, H. Fangohr, K. Giewekemeyer, M. S. Hunter, M. Karnevskiy, R. A. Kirian, H. Kirkwood, Y. Kim, J. Koliyadu, H. Lange, J. Letrun, J. Lübke, T. Michelat, A. J. Morgan, N. Roth, T. Sato, M. Sikorski, F. Schulz, J. C. H. Spence, P. Vagovic, T. Wollweber, L. Worbs, O. Yefanov, Y. Zhuang, F. R. N. C. Maia, D. A. Horke, J. Küpper, N. D. Loh, A. P. Mancuso, H. N. Chapman, 3D diffractive imaging of nanoparticle ensembles using an x-ray laser. *Optica* **8**, 15–23 (2021).

39. T. Stielow, S. Scheel, Reconstruction of nanoscale particles from single-shot wide-angle free-electron-laser diffraction patterns with physics-informed neural networks. *Phys. Rev. E* **103**, 053312 (2021).

40. K. Ayyer, A. J. Morgan, A. Aquila, H. DeMirci, B. G. Hogue, R. A. Kirian, P. L. Xavier, C. H. Yoon, H. N. Chapman, A. Barty, Low-signal limit of X-ray single particle diffractive imaging. *Opt. Express* **27**, 37816–37833 (2019).

41. K. S. Raines, S. Salha, R. L. Sandberg, H. Jiang, J. A. Rodríguez, B. P. Fahimian, H. C. Kapteyn, J. Du, J. Miao, Three-dimensional structure determination from a single view. *Nature* **463**, 214–217 (2010).

42. G. Wang, H. Yu, W. Cong, A. Katsevich, Non-uniqueness and instability of 'ankylography'. *Nature* **480**, E2–E3 (2011).

43. S. Dold, "Time-resolved imaging of laser-induced phase transitions in free silver nanoclusters," thesis, Universität Freiburg (2020).

44. A. Colombo, J. Zimmermann, B. Langbehn, T. Möller, C. Peltz, K. Sander, B. Kruse, P. Tümmler, I. Barke, D. Rupp, T. Fennel, The scatman: An approximate method for fast wide-angle scattering simulations. *J. Appl. Cryst.* **55**, 1232–1246 (2022).

45. Y. Huttel, *Gas-Phase Synthesis of Nanoparticles* (John Wiley & Sons, 2017).

46. K. Engel, B. Laasch, The modulus of the Fourier transform on a sphere determines 3-dimensional convex polytopes. *J. Inverse Ill Posed Probl.* **30**, 475–483 (2022).

47. S. Marchesini, Invited article: A unified evaluation of iterative projection algorithms for phase retrieval. *Rev. Sci. Instrum.* **78**, 011301 (2007).

48. R. Kirian, H. Chapman, *Imaging of Objects by Coherent Diffraction of X-Ray Free-Electron Laser Pulses* (Springer International Publishing, 2020), pp. 1337–1397.

49. B. Erk, J. P. Müller, C. Bomme, R. Boll, G. Brenner, H. N. Chapman, J. Correa, S. Düsterer, S. Dziarzhytski, S. Eisebitt, H. Graafsma, S. Grunewald, L. Gumprecht, R. Hartmann, G. Hauser, B. Keitel, C. von Korff Schmising, M. Kuhlmann, B. Manschwetus, L. Mercadier, E. Müller, C. Passow, E. Plönjes, D. Ramm, D. Rompotis, A. Rudenko, D. Rupp, M. Sauppe, F. Siewert, D. Schlosser, L. Strüder, A. Swiderski, S. Techert, K. Tiedtke, T. Tilp, R. Treusch, I. Schlichting, J. Ullrich, R. Moshammer, T. Möller, D. Rolles, CAMP@FLASH: An end-station for imaging, electron- and ion-spectroscopy, and pump–probe experiments at the FLASH free-electron laser. *J. Synchrotron Radiat.* **25**, 1529–1540 (2018).

50. W. Ackermann, G. Asova, V. Ayvazyan, A. Azima, N. Baboi, J. Bähr, V. Balandin, B. Beutner, A. Brandt, A. Bolzmann, R. Brinkmann, O. I. Brovko, M. Castellano, P. Castro, L. Catani, E. Chiadroni, S. Choroba, A. Cianchi, J. T. Costello, D. Cubaynes, J. Dardis, W. Decking, H. Delsim-Hashemi, A. Delserieys, G. Di Pirro, M. Dohlus, S. Düsterer, A. Eckhardt, H. T. Edwards, B. Faatz, J. Feldhaus, K. Flöttmann, J. Frisch, L. Fröhlich, T. Garvey, U. Gensch, C. Gerth, M. Görler, N. Golubeva, H.-J. Grabosch, M. Grecki, O. Grimm, K. Hacker, U. Hahn, J. H. Han, K. Honkavaara, T. Hott, M. Hüning, Y. Ivanisenko, E. Jaeschke, W. Jalmuzna, T. Jezynski, R. Kammering, V. Katalev, K. Kavanagh, E. T. Kennedy, S. Khodyachykh, K. Klose, V. Kocharyan, M. Körfer, M. Kollewe, W. Koprek, S. Korepanov, D. Kostin, M. Krassilnikov, G. Kube, M. Kuhlmann, C. L. S. Lewis, L. Lilje, T. Limberg, D. Lipka, F. Löhl, H. Luna, M. Luong, M. Martins, M. Meyer, P. Michelato, V. Miltchev, W. D. Möller, L. Monaco, W. F. O. Müller, O. Napieralski, O. Napoly, P. Nicolosi, D. Nölle, T. Nuñez, A. Oppelt, C. Pagani, R. Paparella, N. Pchalek, J. Pedregosa-Gutierrez, B. Petersen, B. Petrosyan, G. Petrosyan, L. Petrosyan, J. Pflüger, E. Plönjes, L. Poletto, K. Pozniak, E. Prat, D. Proch, P. Pucyk, P. Radcliffe, H. Redlin, K. Rehlich, M. Richter, M. Roehrs, J. Roensch, R. Romaniuk, M. Ross, J. Rossbach, V. Rybnikov, M. Sachwitz, E. L. Saldin, W. Sandner, H. Schlarb, B. Schmidt, M. Schmitz, P. Schmüser,

J. R. Schneider, E. A. Schneidmiller, S. Schnepp, S. Schreiber, M. Seidel, D. Sertore, A. V. Shabunov, C. Simon, S. Simrock, E. Sombrowski, A. A. Sorokin, P. Spanknebel, R. Spesyvtsev, L. Staykov, B. Steffen, F. Stephan, F. Stulle, H. Thom, K. Tiedtke, M. Tischer, S. Toleikis, R. Treusch, D. Trines, I. Tsakov, E. Vogel, T. Weiland, H. Weise, M. Wellhöfer, M. Wendt, I. Will, A. Winter, K. Wittenburg, W. Wurth, P. Yeates, M. V. Yurkov, I. Zagorodnov, K. Zapfe, Operation of a free-electron laser from the extreme ultraviolet to the water window. *Nat. Photonics* **1**, 336–342 (2007).

51. H. Haberland, M. Karrais, M. Mall, A new type of cluster and cluster ion source. *Z. Phys. D At. Mol. Cl.* **20**, 413–415 (1991).

52. L. Strüder, S. Epp, D. Rolles, R. Hartmann, P. Holl, G. Lutz, H. Soltau, R. Eckart, C. Reich, K. Heinzinger, C. Thamm, A. Rudenko, F. Krasniqi, K.-U. Kühnel, C. Bauer, C.-D. Schröter, R. Moshammer, S. Techert, D. Miessner, M. Porro, O. Hälker, N. Meidinger, N. Kimmel, R. Andritschke, F. Schopper, G. Weidenspointner, A. Ziegler, D. Pietschner, S. Herrmann, U. Pietsch, A. Walenta, W. Leitenberger, C. Bostedt, T. Möller, D. Rupp, M. Adolph, H. Graafsma, H. Hirsemann, K. Gärtner, R. Richter, L. Foucar, R. L. Shoeman, I. Schlichting, J. Ullrich, Large-format, high-speed, X-ray pnCCDs combined with electron and ion imaging spectrometers in a multipurpose chamber for experiments at 4th generation light sources. *Nucl. Instrum. Methods Phys. Res. A* **614**, 483–496 (2010).

53. J. Miao, D. Sayre, H. Chapman, Phase retrieval from the magnitude of the Fourier transforms of nonperiodic objects. *J. Opt. Soc. Am. A* **15**, 1662–1669 (1998).

54. B. L. Henke, E. M. Gullikson, J. C. Davis, X-ray interactions: Photoabsorption, scattering, transmission, and reflection at *E*= 50-30,000 eV, *Z*= 1-92. *At. Data Nucl. Data Tables* **54**, 181–342 (1993).

55. P. Moscato, C. Cotta, A gentle introduction to memetic algorithms, in *Handbook of Metaheuristics* (Springer, 2003), pp. 105–144.

56. A. Colombo, D. E. Galli, L. De Caro, F. Scattarella, E. Carlino, Facing the phase problem in coherent diffractive imaging via memetic algorithms. *Sci. Rep.* **7**, 42236 (2017).

57. R. Storn, K. Price, Differential evolution—A simple and efficient heuristic for global optimization over continuous spaces. *J. Glob. Optim.* **11**, 341–359 (1997).

58. F. Gao, L. Han, Implementing the nelder-mead simplex algorithm with adaptive parameters. *Comput. Optim. Appl.* **51**, 259–277 (2012).

59. A. Taflove, Application of the finite-difference time-domain method to sinusoidal steady-state electromagnetic-penetration problems. *IEEE Trans. Electromagn. Compat.* **EMC-22**, 191–202 (1980).

60. C. Varin, C. Peltz, T. Brabec, T. Fennel, Attosecond plasma wave dynamics in laser-driven cluster nanoplasmas. *Phys. Rev. Lett.* **108**, 175007 (2012).